Sustainable Energy & Fuels

# Forty-Two Days in the SPA, Building a Stability Parameter Analyzer to Probe Degradation Mechanisms in Perovskite Photovoltaic Devices



| | |
|---|---|
| Journal: | *Sustainable Energy & Fuels* |
| Manuscript ID | SE-ART-03-2023-000327.R1 |
| Article Type: | Paper |
| Date Submitted by the Author: | 30-May-2023 |
| Complete List of Authors: | Dunfield, Sean; University of California San Diego, Nanoengineering<br>Louks, Amy; National Renewable Energy Laboratory (NREL), United States,<br>Waxse, Jay; National Renewable Energy Laboratory, Materials Science Center<br>Tirawat, Robert; National Renewable Energy Laboratory, Chemistry and Nano Science Center<br>Robbins, Steven; National Renewable Energy Laboratory, Materials Science Center<br>Berry, Joseph; National Renewable Energy Laboratory (NREL), United States, National Center for Photovoltaics<br>Reese, Matthew; National Renewable Energy Laboratory, |
| | |

ARTICLE

# Forty-Two Days in the SPA, Building a Stability Parameter Analyzer to Probe Degradation Mechanisms in Perovskite Photovoltaic Devices

Received 00th January 20xx,
Accepted 00th January 20xx

DOI: 10.1039/x0xx00000x

Sean P. Dunfield[a†*], Amy E. Louks[bc], Jay Waxse[a], Robert Tirawat[c], Steve Robbins[a], Joseph J. Berry[a], Matthew O. Reese[a*]

The ISOS protocols provide a robust framework for stability testing and facilitating the description and comparison of results within the community. However, they are not prescriptive on how to achieve the conditions required for degradation. Herein, we discuss various options for satisfying the ISOS light stability series (ISOS-L-#) of tests, a homebuilt testing apparatus that is readily adaptable for decoupling and monitoring stressors in reliability tests, and a homebuilt software suite that is capable of extracting figures of merit over time, cleaning up the data, filtering between data sets, and visualizing the data in several ways. With these, we provide a case study to illustrate the type of data the system produces and an approach to extract degradation mechanisms and/or acceleration factors with such a tool.

## Introduction

Metal halide perovskite solar cells (PSCs) of the form $ABX_3$ – where A is generally methylammonium (MA), formamidinium (FA), or cesium (Cs), B is lead (Pb) or tin (Sn), and X is iodide (I) or bromide (Br) – have recently attracted significant attention from the photovoltaic (PV) community due to their high efficiencies, easy fabrication processes, and tunable bandgaps. However, to be economically viable they must have competitive levelized costs of electricity to other technologies, which depends not only on the initial efficiency and cost of the PV module, but also on its performance over time. Therefore, demonstrating reliable perovskite PV modules to investors will be crucial for commercialization. Specifically, mass commercializing products for grid-level deployment in the near-term will require proof that cells and modules can withstand 20 or more years of operation outdoors in various climates without an equivalent duration of outdoor data. While IEC 61215 provides *qualification* tests for present-day commercial PV technologies, the tests were specifically developed to screen infant mortalities for module-level degradation modes – thus, passing them does not provide a warranty. Warranties are determined by individual manufacturers, usually from more aggressive/comprehensive internal testing, and are ultimately tied to product bankability, with the highest tier manufacturers having better warranties than lower tier manufacturers.

Therefore, it would benefit the community to develop its own set of accepted tests to ensure investor confidence. Ideally these tests would gauge the effect of a specific degradation mechanism by using quantitative acceleration factors to enable prediction of operational lifetimes or lack thereof. However, such insight requires identification of the degradation mechanisms available to the specific device architecture, the stressors that evoke them, and physical models on how reaction rates can be altered with quantifiable rate constants and activation energies. Unfortunately, PSC research is only beginning to identify the degradation mechanisms available to the myriad of device architectures. Consequently, it is of utmost importance that the community starts to use a set of common test conditions to identify and compare degradation among the different architectures utilized.

To facilitate this effort on stability, attendees of the 11th International Summit on Organic and Hybrid Photovoltaic Stability (ISOS) recently updated a set of degradation protocols originally formulated for organic PV[1] to make them more broadly useful to the perovskite community.[2] These protocols, which were released in a consensus statement from many of the largest research groups worldwide, aim to provide a methodical framework for stability testing to ensure that tests are being conducted in an insightful and comparable way. More specifically, the protocols divide testing into six unique stressor categories and three "levels", each with their own ambient and inert condition. The categories are intended to both test for degradation in photovoltaically relevant conditions and separate known stressors such that their effects on device performance can be decoupled; the levels are meant to provide increasing stages of sophistication and stress/difficulty as devices are hardened, with the "inert" and "ambient"

[a.] *Materials Science Center, National Renewable Energy Laboratory, Golden, CO, 80401, USA.*
[b.] *Chemistry Department, Colorado School of Mines, Golden, CO, 80401, USA.*
[c.] *Chemistry and Nanoscience Center, National Renewable Energy Laboratory, Golden, CO, 80401, USA.*
[†] S.P.D. is currently affiliated with the Department of Nanoengineering, University of California San Diego, La Jolla, CA, 92093, USA.
Electronic Supplementary Information (ESI) available: software details, additional degradation plots. See DOI: 10.1039/x0xx00000x

specifications enabling further tuning of stressors. This creates several test specifications, such as ISOS-D1-I, that contain a singular stressor and provides an official framework for measuring intrinsic degradation (e.g., from factors that are unavoidable for a PV device under normal expected operating conditions) in a situation where extrinsic factors that could otherwise dominate degradation (e.g., $O_2$, $H_2O$, encapsulant) are eliminated. Ideally, by comparing results from these standardized tests, the community can gain an understanding of what stressors initiate specific degradation mechanisms in perovskites, allowing protocols that accelerate and screen for a given degradation pathway to be developed.

While the ISOS protocols provide a robust framework for stability testing and separating stressors, it is important to realize that they are merely a set of aging schedules to facilitate the description and comparison of results within the community. Consequently, two distinct methods of using the protocols have emerged in the literature: some studies use them to optimize stability by iteratively improving the degradation *modes* of their devices with little insight besides overall power output over time, others take them one step further to couple the degradation *modes* to first a *stressor* and then ultimately propose a *mechanism* or set of mechanisms which can be further investigated. Herein, we lay the groundwork for the latter type of study. To do so, we first describe various options for satisfying ISOS conditions, a homebuilt testing apparatus that is readily adaptable for decoupling and monitoring stressors in reliability tests, and a homebuilt software suite that is capable of extracting figures of merit over time, analyzing the data, and extracting trends; then we provide a case study to illustrate an approach to extract degradation mechanisms and/or acceleration factors with such a tool along with some useful ways of visualizing the data. As one of the most challenging set of aging schedules to establish and analyze are the light/laboratory tests (ISOS-L#-I),[1,2] we explicitly focus on discerning the intrinsic photoactivated degradation behavior in an *indium doped tin oxide [ITO] / Poly[bis(4-phenyl)(2,4,6-trimethylphenyl)amine] [PTAA] / $MA_{0.08}FA_{0.87}Cs_{0.05}Pb(I_{0.92}Br_{0.08})_3$ / carbon 60 [$C_{60}$] / tin oxide [$SnO_x$] / silver [Ag] device architecture*. To do so we explore stability of devices under ~ 1 sun illumination, near maximum power point (MPP), in $N_2$, at 33, 50, 65, and 85 ˚C. This allows us to discern the intrinsic stability of the device, and, because standard test conditions are used, benchmark the results versus other devices.

## Experimental

An ideal degradation setup stresses samples using five main factors: light, bias, temperature, humidity, and oxygen. For our setup, we divided these stressors into three independent parts: the light source, electronics, and environmental control/housing. This creates a modular system with components that can be interchangeably swapped out, allowing comparisons between different components (such as type of light source, bias point, type of test run, or environmental conditions) and updates to our system as the important details of degradation/stressors are converged on by the community. This system must then be coupled with a set of algorithms to extract relevant figures of merit and averages from the raw data to identify trends and develop hypotheses on the root cause(s) for degradation. We will begin our discussion with light sources.

**Light Source.**

The ISOS protocols[2] state that "ideally, light sources with an irradiance of 800-1000 W $m^{-2}$ (1 sun = 1000 W $m^{-2}$) should be applied, and the exact irradiance, the type of light source, and its spectrum should be reported." Moreover, they recognize that options for light sources vary greatly and suggest that particular attention should be focused on the spectrum of the light and its drift over time. Thus, the ISOS protocols, except for ISOS-L3 where a deviation from the solar spectrum is specified, allow for a range of light source options. In the perovskite community, this has resulted in the use of five main light source types: sulfur plasma,[3–6] tungsten halogens,[4,7,7,8] light-emitting-diodes (LEDs),[3,4,7,7,9–11] metal halides,[3,7,7,8,12,13] and xenon arc lamps.[7,7,8] **Figure 1A** shows example spectra of these options next to the perovskite-absorbed and -unabsorbed sections of AM1.5G. As can be seen, most options are unable to mimic the solar spectrum across the entire range of irradiance but provide adequate intensity over most of the region where single junction and widegap perovskites are expected to absorb light. Therefore, if one wants to observe the effect of standard charge generation and extraction in devices, almost any light source will do, but if the goal is to probe UV or IR induced degradation, a more particular light source is necessary (e.g., in the case of tandems). However, just as important as the spectrum of the light, is how long it can be maintained without drift or catastrophic failure. This varies greatly from source to source but is generally the worst in the case of metal halide and xenon arc lights.[7,7,7,14] Thus, while metal halide and xenon lights are common for solar simulators, which require a very specific spectrum over short periods of time, other light sources are commonly used for degradation testing setups. As a result, there is not a clear "winner" in terms of light sources. Rather, the light source should be chosen for the test desired. A list of pros and cons for various light sources are displayed in **Figure 1B**. As can be seen, no light source is ideal. This gets further convoluted as one starts trying to make the light sources uniform over a large area due to differences in light source type (point vs. area), fixtures (ballast vs. array), and native uniformity. Due to these mandatory trade-offs associated with each of the light sources, our two stability parameter analyzer (SPA) systems currently use identical electronics and environmental control/monitoring to each other, but with different light sources: sulfur plasmas, due to their reasonable accuracy across the entire spectrum, and a homebuilt LED lamp, due to its low price, lack of spectral drift, and facile process to make uniform. This allows us to use the inexpensive LEDs to get far better statistics and use the more expensive sulfur plasma lamp in cases where the spectrum is likely to make a large difference, such as in monolithically connected tandems where the top and bottom cells must be current matched.

 

A)

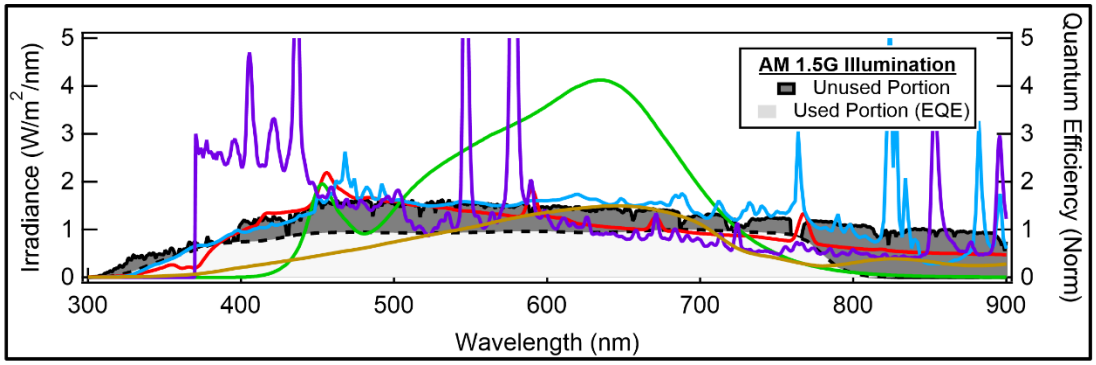


B)

| Classification | | Spectrum | | Cost | | | Additional Information | |
|---|---|---|---|---|---|---|---|---|
| Source Name | Source Type | Intensity Fluctuation | Spectral Drift | Total Cost | Service Life | Additional Equipment | Pros | Cons |
| Sulfur Plasma | Light Emitting Plasma | Small | Small | $$ | Long | RF Magnetron, Waveguide | Lifetime, brightness, spectrum, stability at various powers | Difficult to reach class A uniformity |
| Tungsten Halogen | Incandescent (Filament) | Small | Medium | $$ | Short | Start Circuit, Power Supply | Short-term stability, compactness | Fire, Requires optical filter for IR |
| White LEDs | Light Emitting Diode | Small | Small | $ | Long | Power Supply | Rapid on/off, dimmable, lifetime, tunable | Limited spectral range from singular LED |
| Xenon Arc | High Intensity Discharge | Large | Large | $$$ | Short | Ballast, Ignitor | Spectrum, brightness | Explosion, Ozone, IR spectral lines, Requires alignment & optical filter |
| Metal Halide | High Intensity Discharge | Medium | Medium | $$$ | Medium | Ballast, Ignitor, Power stabilizer | Tunable, brightness | Explosion, Ozone, Spectral lines, mercury, Requires optical filter |

**Figure 1. Common Light Sources for Degradation Testing. A)** Spectral Irradiance for popular light sources in relation to the absorbed and unabsorbed portions of AM1.5G. All sources were measured at the National Renewable Energy Laboratory. **B)** Tabulated information useful for selecting a light source for a sulfur plasma,[3–6] tungsten halogens,[4,7,7,8] white light-emitting-diodes (LEDs),[3,4,7,7,9–11] metal halides,[3,7,7,8,12,13] and xenon arc lamps.[7,7,8]

**Electrical Monitoring.**

The second set of choices that need to be made pertain to the electronics, as the ISOS protocols[2] allow for a range of bias and measurement options. For biasing, they allow levels one and two to be satisfied by either open circuit conditions, where the devices terminals are left unconnected, or near MPP conditions, where the device would ideally be during most of operation. It is noteworthy that while these conditions are often very similar in terms of the applied voltage, the latter (near-MPP/MPP) will have a substantial amount of current flowing through the device while the former will have none. Therefore, the tests could have drastically different results, making MPP preferred and even required in the case of ISOS-L3. However, these conditions are more difficult to achieve. The main method to do so, and the only way to fulfill the third level, is to apply a perturb and observe MPP tracking algorithm.[15–17] But, doing so requires a dedicated circuit per cell and thus adds a level of complexity and cost. Another way to make a very good approximation, but at a much cheaper price point, is to use a fixed load.[1] This can be done by either fixing the voltage between the terminals of the cell to be constant or connecting them to a load line (resistor) that biases the device at the voltage where its IV curve intersects the resistor, as shown in **Figure 2A**. It should be noted that while these methods clearly forgo control of the exact bias point, they allow both currents and voltages very similar to MPP conditions to be obtained very cheaply. To illustrate this, the expected deviation between MPP and the bias point for a 510 Ohms resistor is shown for a hypothetical ~18% starting cell in **Figure 2B**. As can be seen, significant deviation from the starting parameters is required to push the cell substantially away (>10%) from MPP conditions. Moreover, this degradation must occur non-uniformly across the measurable device parameters – short circuit current density ($J_{sc}$), open circuit voltage ($V_{oc}$), and fill factor (FF). For this reason, we chose to utilize resistor loads in our setup, although we did so in a way that allows us to replace each of the resistors with a trim pot and fixed resistors, digital potentiometer, or true MPP tracking circuit, if desired. Experimental data from the system, shown in **Figure 2C**, confirm the general validity of this approach, albeit suggest that different resistors will likely be required for different starting parameters.

With a bias strategy chosen, the next decision that needs to be made is how the cells will be characterized. In regard to this, the ISOS protocols[2] simply state that “due to the ongoing development of best practices for measuring J-V [current voltage] curves and the efficiency of PSCs, the procedure of making periodic measurements during aging tests should be clearly described.” However, we note that unless one wants to

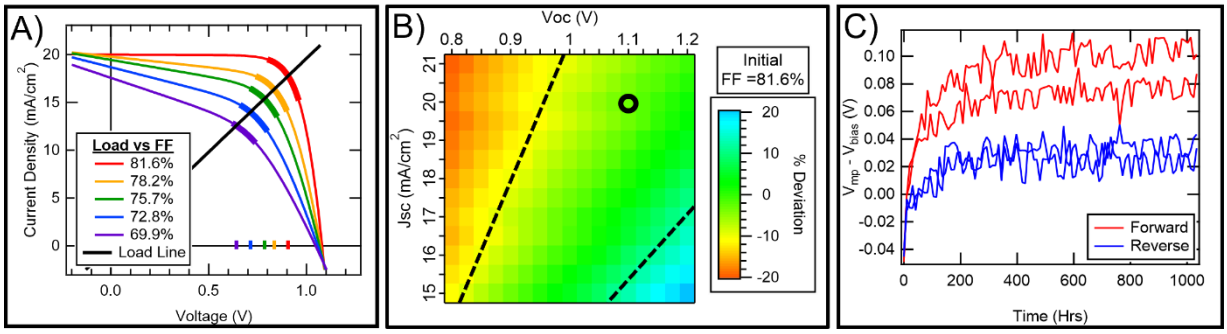


**Figure 2. Modelling and experimental results show that biasing with a resistive load holds the devices near MPP. A)** JV curves versus load line for devices with a variety of FF's obtained by altering the series and shunt resistance. Thicker portions of JV traces indicate ±10% of MPP. The bias held across each device is the voltage at which the resistor load intersects the JV curve and is indicated by the vertical lines on the x-axis. **B)** Modelled deviation between the maximum power point and a 510 Ohm resistive load bias point for a range of $J_{sc}$ and $V_{oc}$ losses (series and shunt resistance held constant). **C)** Experimental deviation between the maximum power point resistive load for an example device with ~16 mA/cm$^2$ $J_{sc}$, ~1 V $V_{oc}$, and ~69% FF.

use only MPP tracked data, which is not particularly insightful for diagnosing the cause(s) of degradation, it will be essential to have the ability to remove the load used for aging to perform some other characterization. This can be done in three main ways: 1) by using a dedicated line/source measure unit (SMU) for each channel, 2) by using a multiplexer (aka mux) that can connect *one* channel (the SMU) to *n* options (the devices), or 3) by using a matrix that can connect *m* channels to *n* options. The first option is akin to a standard solar simulator and provides maximum versatility but is generally cost prohibitive and limits the number of channels that can be measured. The second option allows the number of SMUs to be reduced from the number of pixels to just one, providing a substantially more cost-effective alternative that can characterize the devices in-situ. However, it restricts the number of characterization techniques that can be applied to a singular channel, which may be limiting in the future. In contrast, the third option allows for each of the devices to be connected to several different measurement techniques. Since changing out the set of electronics is far more complicated than the light source (largely due to software requirements), we decided to invest in this third option, giving us maximal capability to expand in the future. It should be noted that while we are currently only using this function to run current voltage JV or MPP measurements, it would be trivial to expand the system to do other electronic measurements, such as capacitance-voltage measurements. However, we currently find the JV curves to provide significant insight and are not confident in the non-perturbative nature of other possibly insightful measurements. In this direction, given that substantial literature has shown that applied voltage can affect perovskite degradation,[18–20] even the JV sweeps themselves could be altering degradation.

**Temperature & Ambient Control.**

Using the components described above with a scheme to contact devices, one can start conducting basic experiments to compare device degradation. For example, the setup can be used in a glovebox to compare the intrinsic stability of a group of cells. However, while these measurements may be useful for comparing among a singular data set, they are not as useful to the community as they could be for comparing among different data sets because they lack information about the environment and details of the setup. For example, without monitoring the light intensity of the setup, which can evolve over time, $J_{sc}$ losses can be contributed to either a reduction in the generation and extraction capabilities of the cell or to a smaller amount of incident light from which the cell can absorb. Thus, to be maximally relevant to others and ensure that false conclusions are not made, the ISOS protocols recommend that setups have the ability to at least monitor degradation factors that may fluctuate, but ideally control them as well.[1,2] In our setup, we did this using the overengineered environmental housing unit pictured in **Figure 3A**, which can test up to 12 x 1 in$^2$ substrates with up to 4 pixels each**.** As can be seen, the unit – dubbed a 'flow tube' – consists of numerous features that, in contrast to a glovebox environment, allow the cells environment to be monitored and tailored between ambient and inert. The outside is comprised of a long borosilicate glass tube with metal endcaps that have several feedthroughs. On the right-hand side we have an inlet for gas (blue arrow), an inlet and outlet to the copper tubes which run along the inside for temperature control (orange arrows), and a passthrough for our electronics

A)

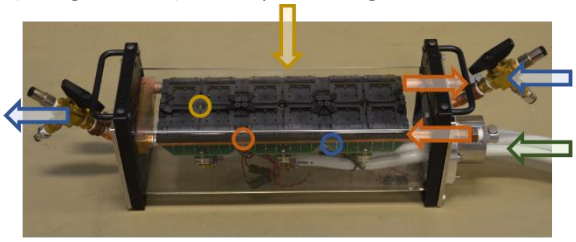

B)

| Stressor | Control (⟸) | Monitor (○) |
|---|---|---|
| Atmosphere | $N_2$/Dry Air/Air | Relative Humidity |
| Temperature | Heater/Chiller | Temperature |
| Light | External Light | Intensity |
| Bias | Passive | Bias Voltage |

**Figure 3. Environmental housing unit. A)** Hardware used to control and monitor the atmosphere, temperature, light, and bias of the cells during degradation. Each black quad block is 3.2 x 3.25 in. **B)** List of stressors along with how they are controlled and monitored.

(green arrow). Then, on the left-hand side, we have a 2.5 psi pressure release valve and a one-way exit valve for the gas (blue arrow). The inside of the tube consists of several metal sample holders with pogo pins pushing through the bottom to make electrical contact to the cells, copper tubes to carry water from an external heater/chiller (e.g. Thermo Scientific Artic A25 Refrigerated Bath Circulator) through the metal sample holders to control their temperature, and a series of sensors to monitor degradation stressors. Specifically, the unit employs a Honeywell HIH-4000 sensor to monitor the humidity (blue circle), a PT1000 resistive thermal detector (RTD) to monitor the temperature (orange circle), and a Hamamatsu S1133-01 Silicon photodiode to monitor the light intensity (yellow circle). With a constant light source spectrum and reliable gas sources coming from the house gas lines, this setup affords us the ability to both control known stressors and monitor the ones which may reasonably vary. These stressors, the way they are controlled, and the type of monitoring used are summarized in **Figure 3B.** We note that while this system works well, the custom environmental flow tubes could likely be replaced by off-the-shelf, metal, washdown electrical enclosures with a window (e.g. ones with an IP66 and NEMA 4 rating) to achieve a much lower price point while still maintaining sufficient environmental control.

**Modular Assembly & Calibration.**

Once the individual parts are built, the next step is to put them together and optimize the system. This involves optimizing the uniformity and intensity of the light source across the sample analysis area and running control tests to ensure that everything is working. Pictures showing our assembled SPA setup using both the sulfur plasma lamp and LEDs as the light sources are shown in **Figure 4A** and **4B**, respectively**.** Another photo showing an overhead view of the assembled LED-based degradation system is shown in **Figure 4C.** A schematic further detailing how the electronics work for each quad block of cells (each with 4 pixels) is shown in **Figure 4D.** It is worth noting, that each device on a shared substrate is electrically isolated from the others so that there is no crosstalk. This is especially important when one sample is being measured and others have a load applied. As can be seen in **Figures 4A-C** and **4E**, a significant amount of hardware has been added to ensure uniformity of the light sources and reproduceable positioning of the cells underneath them. This hardware consists of several main features: 1) a method to mount and cool the light source a set distance above the environmental chambers, 2) a fixture to ensure reproduceable placement of the environmental chamber underneath each light source, and 3) reflectors to improve the uniformity *and intensity* of the light source. We note that while setting up (1) and (2) are fairly trivial and subject to change depending on how the system is connected, (3) requires significant effort and is of utmost importance. To illustrate this point, we have displayed a picture of the optimized LED light source, its uniformity without any reflectors, with unoptimized reflectors, and after careful optimization of the reflectors in **Figures 4E**. As can be seen, the addition of diffuse reflectors improves the uniformity of the light source from ±20% to ±3%, making it meet Class B specifications for the spatial uniformity of a light source.[21] We note that in all setups this is essential to ensure that devices are aged under similar stress from light. However, in our setup and others that choose to utilize resistive loads to apply the bias, the importance of this step is amplified as the bias applied scales with the current of the cell and therefore the light intensity.

The final step before the equipment is ready to test samples is to calibrate the sensors. Generally, the relative humidity and temperature sensors come pre-calibrated with a set of look up tables to convert their readings to useful values. For humidity, simply reporting these values should be sufficient. However, for temperature, an additional calibration factor between the sensor reading and the nominal operating cell temperature (NOCT) is needed, as the two can readily deviate by up to 20 ˚C depending on the light source utilized and sensor location relative to the cell.[22] While this factor is dependent on gas flow rates, light intensity, and heater/chiller setpoints, it can be calibrated by simply measuring the difference between a thermocouple on the cells surface and the sensor reading under the desired conditions. In contrast, calibration of the light source requires the absolute spectrum of the light, the relative external quantum efficiency (EQE) of the photodiode, and the relative EQE (or at least representative EQE) for the cell in order to calibrate a mismatch factor between the intensity *seen* by the diode and that *seen* by the cell.[14,21] While Si photodiodes are a good choice due to their availability, cost, and general stability, care should be taken to use ones in a light impervious, non-reflective package to minimize stray light/backside collection. Additionally, using a color filter (e.g., KG2) can be helpful to make a Si reference more closely mimic the responsivity of a PSC, and bring the mismatch factor closer to unity. This becomes increasingly useful if the light spectrum is expected to change in a region where the cell and the diode have different responses, which causes the mismatch factor to evolve with time.[14] Moreover, it puts a premium on light sources which uniformly decay in spectrum, such as LEDs and sulfur plasma lamps, as opposed to those which have spectral drift, as the calibration factors calculated can remain constant over 1000s of hours.

**Analysis Framework.**

To analyze JV data over time (**Figure 5A**) and organize it in a way conducive to extracting trends, we developed a set of algorithms, methods, and filters that are detailed in **Supplementary Note 1**. These algorithms begin by calculating useful device metrics – such as the power conversion efficiency (PCE), short circuit current density ($J_{sc}$), open circuit voltage ($V_{oc}$), and fill factor (FF) – from the JV curves over time to enable richer insight into the dominant degradation modes and associated mechanisms that may be at play (red circles in **Figure 5B**). Then, they clean up the data by both removing any initial burn in behaviors that may result from sample handing/preconditioning as well as removing unwanted dropouts that occur from miscommunications with

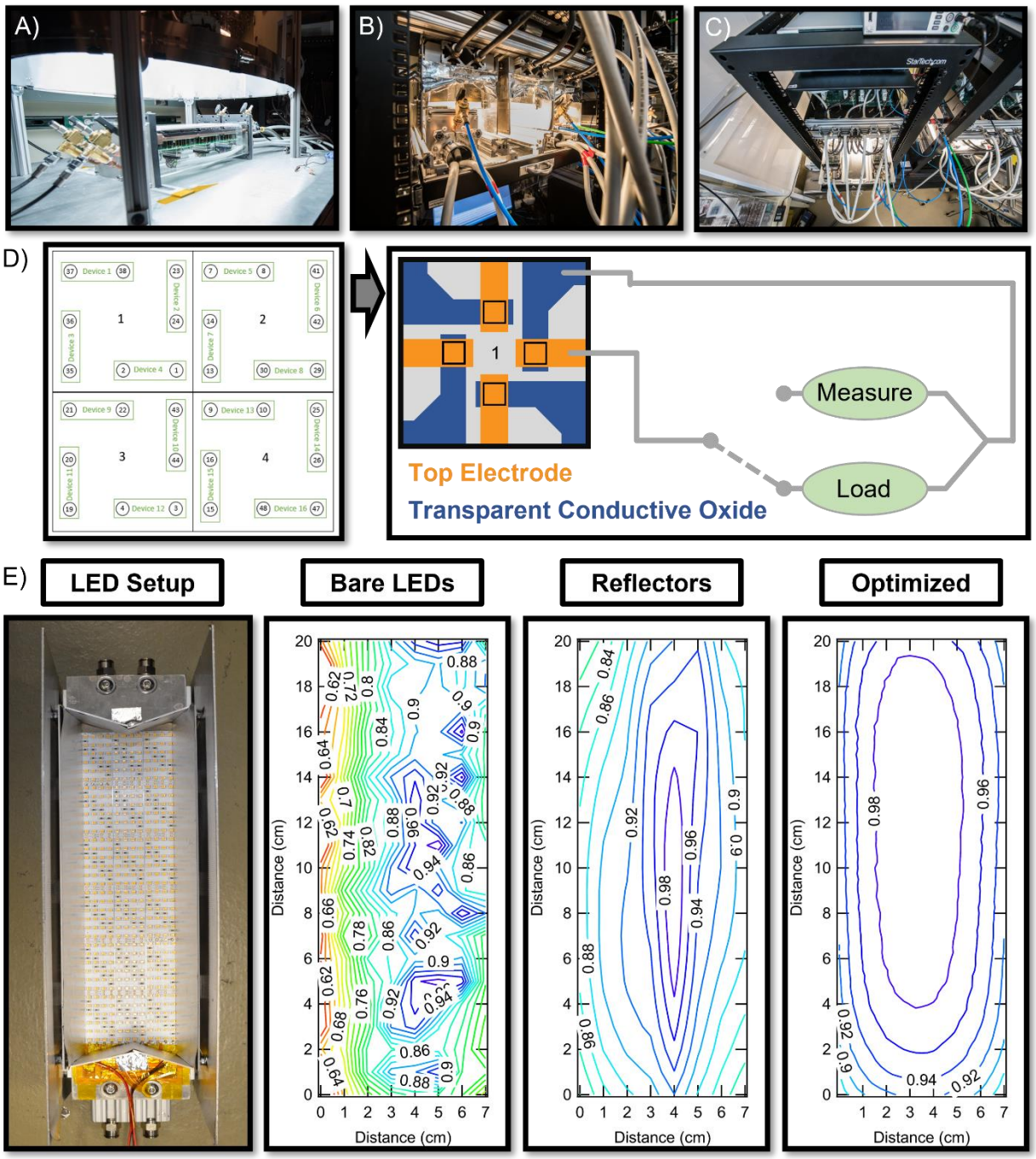


**Figure 4. Details of the SPA setup. A)** Closeup of the sulfur plasma lamp SPA setup. **B)** Closeup of the LED SPA setup showing the mounting structure used to achieve reproducible positioning of the flow cells underneath the light sources and the water cooling lines used for the LED lights. **C)** Overhead view of the LED SPA system showing its incorporation into an electronics rack that houses all components and allows the flow tubes to be loaded/unloaded reproducibly and easily via a drawer. **D)** Schematic of how the system makes contacts, biases, and characterizes the devices. **E)** Photo of the LED light source with graphs of its uniformity without any reflectors, with reflectors, and with careful optimization of the reflectors.

instruments. With the cleaned-up data (yellow plus signs in **Figure 5B**), the kit fits the parameters with a tenth-degree polynomial to determine a best fit line (black line in **Figure 5B**) and produces normalized parameters over time. The purpose of this polynomial fit is to enable good data fidelity for future data manipulation without requiring large amounts of computational overhead, it is not meant to have any physical meaning. Using these interpolated best fit lines for each parameter, the kit then calculates the mean and standard deviation from the mean for each device type to generate a trend line and confidence interval (**Figure 5C**), which can then be compared with other device types (**Figure 5D**). Additionally, it calculates several useful metrics, such as the difference between the MPP of the JV curves and the load applied, the loss in parameters as a summation or function of individual losses (discussed later), the functional form for each degradation

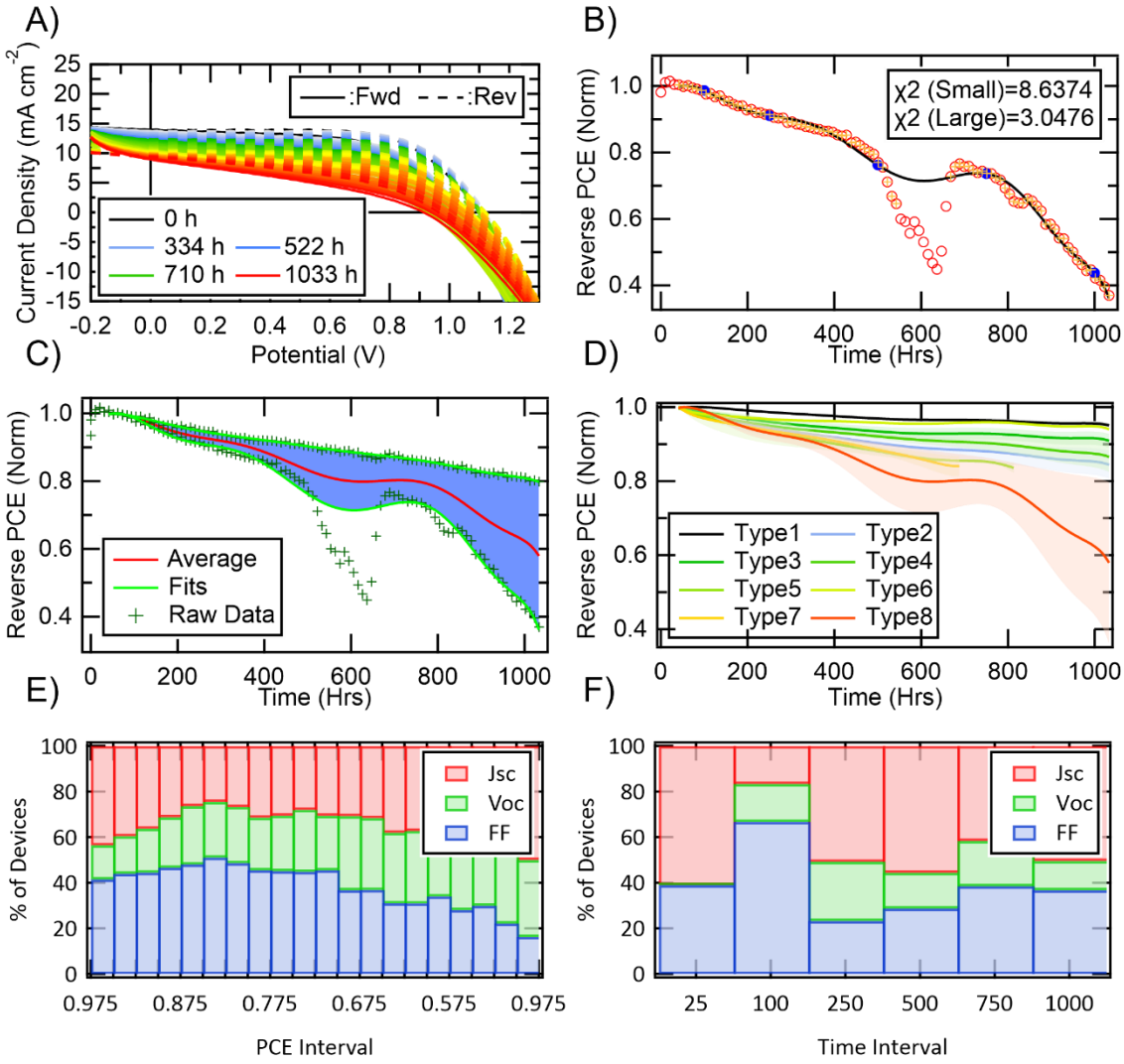


**Figure 5. Standard Data Analysis and Visualization Options. A)** Waterfall plot of JV curves over time. **B)** Extracted figures of merit over time with dropouts removed where $\chi^2$(Large) refers to the $\chi^2$ for a 10$^{th}$ degree polynomial fit and $\chi^2$(Small) refers to the $\chi^2$ for a 4$^{th}$ degree polynomial fit. **C)** Best fit line and confidence interval for two analogue samples of the same type. **D)** Comparison PCE across several different device types with varied architecture. **E)** Binned dominant loss mechanisms versus PCE loss interval, and **F)** binned dominant loses mechanisms extracted from forward scans versus time interval for devices tested at NREL on the SPA from 2017-2020.

mode (linear, polynomial, dual polynomial), and the dominant mode of degradation over various power loss (**Figure 5E**) and time intervals (**Figure 5F**) – determined by which parameter had the largest decrease in normalized parameter across the interval (e.g. $FF^{norm}$(25 h) - $FF^{norm}$ (100 h)) . Finally, although not utilized here, the kit can also filter by device architecture, test duration, test temperature, etc. and easily graph any parameter versus any other parameter for select devices. It should be noted that while we have found the algorithms to be very useful, we ultimately have steered away from using the kit due to Igor Pro's memory usage, which can make analyzing larger datasets cumbersome and prohibit numerous large datasets from being analyzed simultaneously without some sort of data loss. Still, the similarity of Igor Pro's scripting language to C and Python should make porting these methods relatively straightforward to other environments.

## Results & Discussion

With a fully functioning and calibrated stability parameter analyzer and analysis kit, we tested the operational stability of *ITO / PTAA / Perovskite / $C_{60}$ / $SnO_x$ / Ag* devices in $N_2$ at 33, 50, 65, and 85 ˚C (see Supplementary Information for fabrication details). To initialize the tests, devices with active area 0.12 cm$^2$ were loaded unmasked into flow tubes while inside of a solvent-free $N_2$ glovebox with low $O_2$ and $H_2O$ content (< 5 ppm), closed off from the external environment, and then moved to the LED light source/testing apparatus displayed in **Figure 4b-e**. The devices were then attached to the closed-loop temperature control lines (33, 50, 65, and 85 ˚C), exposed to $N_2$, and allowed to equilibrate for 24 h before turning on the light source and starting the experiment. Over the course of the experiment,

environmental stressors were stable (see **Figure S1** for representative sensor readings) and devices were characterized via forward and then reverse scans at a rate of 0.87 V/s with a 10 ms dwell and requests for scans every 30 minutes (subject to hardware availability).

Data for each pixel are shown in the **Supplementary Information**, including waterfall plots of each pixel's JV data over time in **Figures S2-5**, extracted fit parameters for each pixel over time with the average/standard deviation of the grouping indicated in **Figures S6-9**, and the same parameters normalized to their maximum efficiency over the first 24 h of testing in **Figures S10-13**. For comparison purposes, the normalized average and standard deviation of each parameter is plotted against the other temperatures in **Figure 6**. As can be seen, the devices stressed at 33 ˚C show reasonable stability metrics, decaying to roughly 85%/80% of their initial reverse/forward scan PCEs over ~1075 h of testing, almost entirely due to a decrease in the $J_{sc}$. Increasing the temperature to 50 ˚C caused the performance of the devices to decay more quickly, resulting

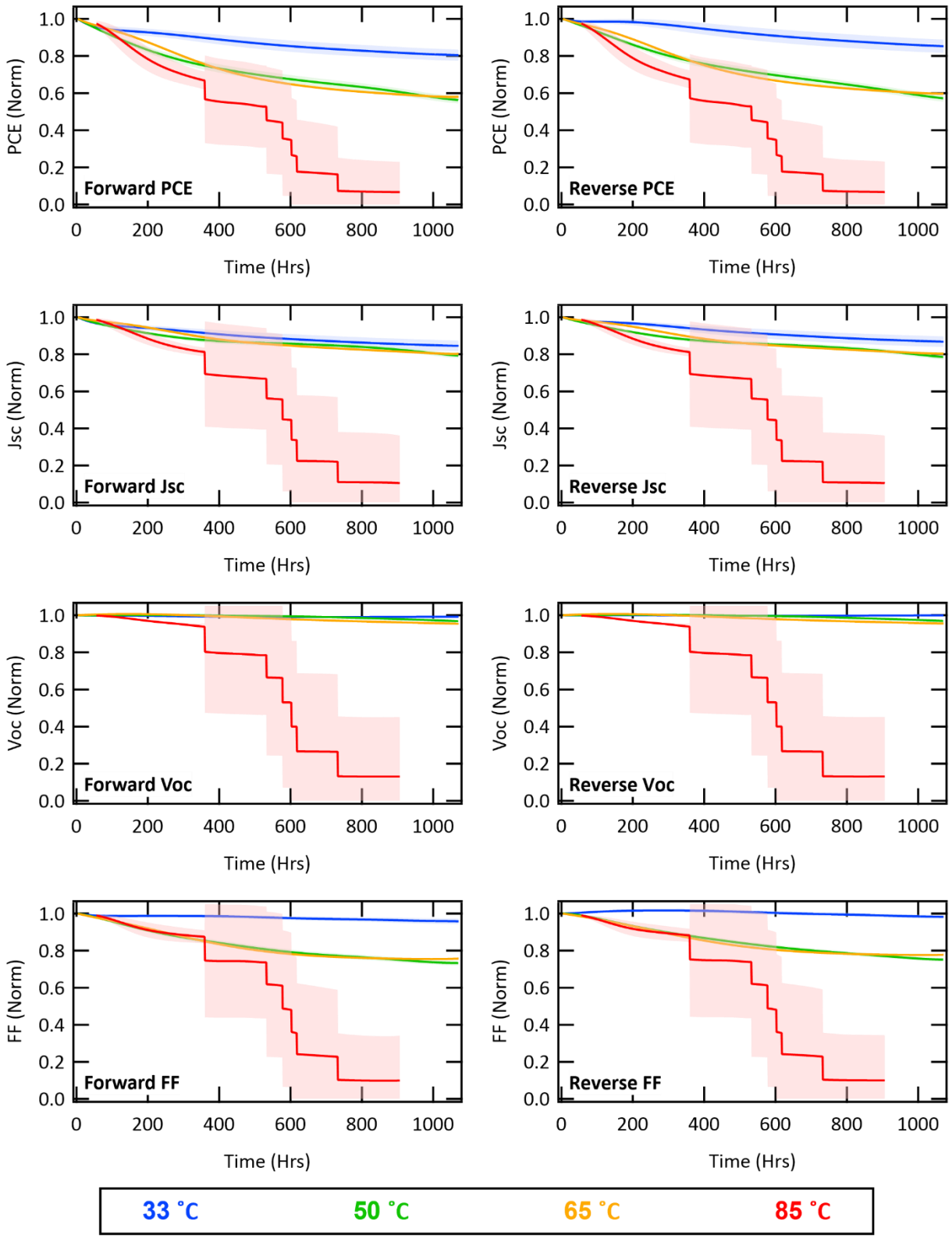


**Figure 6. Normalized Photovoltaic Parameters Over Time.** Normalized forward (left) and reverse (right) power conversion efficiency (PCE), short circuit current density ($J_{sc}$), open circuit voltage ($V_{oc}$), and fill factor (FF) over time for cells degraded near MPP in $N_2$ at 33 ˚C (blue), 50 ˚C (green), 65 ˚C (orange), and 85 ˚C (red) under white LEDs.

in devices which maintained roughly 60% of their initial forward/reverse scan PCE over the same duration due a faster decrease in $J_{sc}$ coupled with a decrease in FF. Interestingly, further increasing the temperature to 65 ˚C did not substantially

change the degradation mode, and if anything, slightly *decreased* the rate of degradation from the 50 ˚C case. Finally, increasing the temperature to 85 ˚C caused the devices to start displaying a decrease in all parameters, followed by catastrophic failure (each step in the staircase-like data beginning around 400 h corresponds to failure of an individual cell). Therefore, it is apparent that the temperature of aging largely impacts the degradation, with 85 ˚C resulting in catastrophic failure, an increase in temperature from 33 to 50 ˚C altering the mode of degradation, and an increase from 50 to 65 ˚C having limited impact on degradation rates or modes. Due to this, we must have two or more competing degradation mechanisms with different activation energies, and an Arrhenius model – which assumes a singular degradation mechanism and mode that is accelerated by temperature – clearly will not fit the data (for an example of Arrhenius behavior see here[23]).

To get a better understanding of how the degradation mode was changing as a function of temperature and time, we averaged the forward and reverse parameters for each pixel and visualized the degradation of parameters in two different ways. First, we visualized the FF, $V_{oc}$, and $J_{sc}$ contributions to PCE loss as a function of time by representing the normalized loss in PCE over time as the summation of losses in other parameters (**Figure 7**), e.g. for $J_{sc}$ loss:

$$J_{sc}^{\%\,Loss} = PCE^{\%\,Loss} * J_{sc}^{nl} * (J_{sc}^{nl} + V_{oc}^{nl} + FF^{nl})^{-1}$$

where $A^{nl}$ is the normalized loss for the parameter 'A' (e.g. Jsc), such that:

$$PCE^{\%\,Loss} = J_{sc}^{\%\,Loss} + V_{oc}^{\%\,Loss} + FF^{\%\,Loss}$$

and the overall PCE and time axes were preserved. Second, we visualized the correlation between the rate of change for each figure of merit and PCE by taking the derivative of the normalized FF, $J_{sc}$, and $V_{oc}$ with respect to the normalized PCE and plotting it as a function of the normalized PCE (**Figure 7**). As can be seen in the left-hand plots, all devices display an overall degradation in PCE that most closely resembles a biexponential with $J_{sc}$ loss contributing heavily at all temperatures, FF playing a substantial role at temperatures above 50 ˚C, and $V_{oc}$ loss increasing with time and temperature. Looking at the right-hand plots, it is apparent that $J_{sc}$ dominates degradation for the 33 and 85 ˚C cases while FF contributes to just over half of the degradation for the 50 and 65 ˚C cases. Moreover, for the devices with sufficiently large degradation, at about 75% remaining PCE the $V_{oc}$ appears to start playing an increasingly large role in degradation while the relative contributions of $J_{sc}$ and FF mirror each other, with the dominant mode becoming more and then less dominant, resulting in the second most dominant parameter ($J_{sc}$ for 50/65 ˚C and FF for 85 ˚C) becoming the most dominant. These profiles illustrate the existence of complex competing mechanisms, each with different activation energies and temperature dependencies.

Although further pre- and post-mortem analysis outside the scope of this work would be required to truly diagnose the degradation mechanisms present in these devices, the degradation modes observed can be extremely insightful. More specifically, $V_{oc}$ is generally affected by non-radiative recombination; $J_{sc}$ by carrier generation and extraction efficiency; and FF by series resistance (resistance along the diode), shunt resistance (resistance opposite to the diode), the ideality factor (the type of recombination in the device), altered interfaces, or mobile ions. Here, we see $J_{sc}$ loss at all temperatures and timescales, FF loss at elevated temperatures, and $V_{oc}$ loss at the highest temperatures and longest timescales. For the most part, these parameters seem to decay in an approximately bi-exponential fashion with different time constants, suggesting multiple degradation pathways. They also coincide with a sharp increase and then slow decrease in the hysteresis between $J_{sc}$ and $V_{oc}$ (**Figure S14**), which has generally been associated with a change in mobile ion concentration. Finally, there appears to be a slowly decreasing shunt resistance as well as slowly increasing characteristic and series resistances in all samples that strongly correlate to the change in FF (**Figure S15**).

Cumulatively, these trends suggest that at all temperatures, interfacial reactions occur that lead to a decrease in extraction efficiency, which negatively impacts $J_{sc}$ and increases the concentration of mobile ions, causing additional hysteresis. At 33 ˚C, the creation of mobile ions appears to hinder decay of other parameters (from approximately 25 to 200 h) until a certain concentration is reached, at which point the hysteresis decreases, $J_{sc}$ loss resumes, and FF loss starts. Presumably, after some concentration of mobile ions is reached, they start altering the interfaces and their extraction capasbilities, leading to loss in FF while minimally affecting $V_{oc}$ (e.g., forming minimal non-radiative recombination centers at the interface). However, at temperatures of 50 and 65 ˚C, the increase in hysteresis is not as pronounced and FF loss starts almost immediately, followed by $V_{oc}$ loss after substantial degradation has occurred. This indicates that increasing the temperature affords a new degradation mode or lowers the concentration of species required to alter the interface negatively. Moreover, it suggests that after substantial degradation of the interface occurs, non-radiative defects begin to form that limit $V_{oc}$. Finally, increasing the temperature to 85 ˚C leads to the immediate loss in all parameters followed by catastrophic failure of the device. Given that the FF, $J_{sc}$, and $V_{oc}$ losses appear to follow the same trends or sequence as the previous cases, we speculate that the catastrophic failure not seen in the other tests is likely through some new mechanism – potentially thermal instability of the PTAA contact or diffusion of the metal into the perovskite. To better understand the exact degradation mechanisms for another iteration of devices, pre- and post-mortem photoluminescence, transient absorption/reflection, and TOF-SIMS could be useful for understanding quasi-Fermi level splitting, carrier diffusivity and lifetimes at the interfaces, and chemical diffusivity, respectively.

 

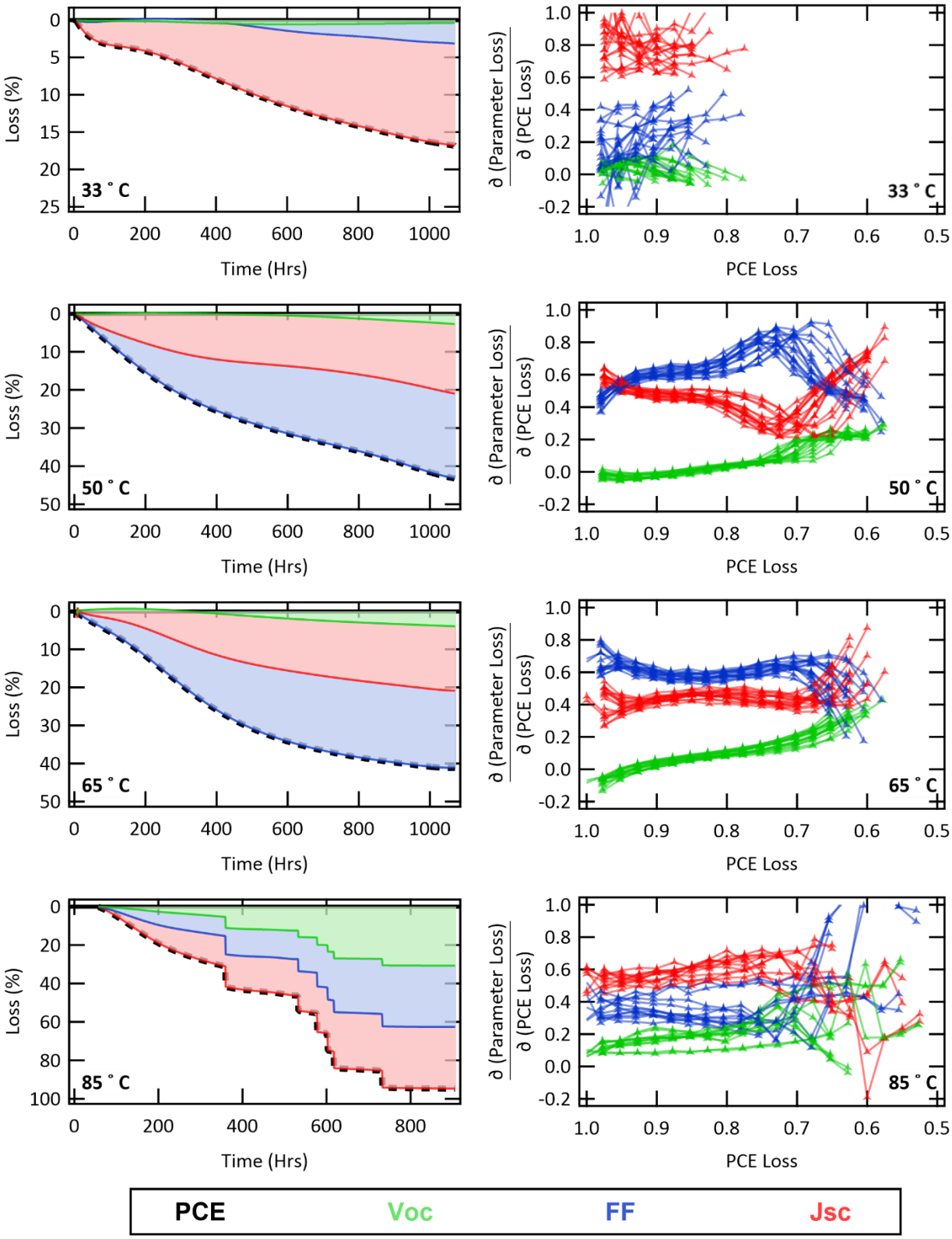


**Figure 7. Visualizing Losses.** (Left) PCE loss with visualization of component losses ($V_{oc}$, FF, and $J_{sc}$) for samples aged at 33, 50, 65, and 85˚C from top to bottom. (Right) Relative parameterized losses for samples aged at 33, 50, 65, and 85˚C from top to bottom. All samples were degraded near MPP in $N_2$ under white LEDs.

## Conclusions

Herein, we have detailed many of the considerations that need to be taken when analyzing the degradation of perovskite solar cells, presented a degradation tool capable of inducing and

monitoring those stressors that is being used regularly at NREL (and different aspects could readily be implemented elsewhere), introduced a series of analysis methods to extract and visualize degradation trends, and detailed a set of degradation tests meant to be illustrative. As can be seen, the choice to control and monitor stressors as well as take periodic JV scans allows substantially more insight into degradation. More specifically, a wide range of dominant degradation modes can be seen depending on aging conditions: at 33 ˚C in $N_2$ device performance is dominated by losses to $J_{sc}$, increasing the temperature to 50-65 ˚C causes FF to dominate, and increasing the temperature further to 85 ˚C causes catastrophic failure of the device. Moreover, these losses are not constant with time. While this large variance in the degradation mode as a function of temperature and time prevents the use of simple and already developed models, such as Arrhenius behavior, analysis of the degradation modes as a function of temperature coupled with a good understanding of device physics can still lead to significant insight on what mechanisms may be dominating. Future work of ours aims to better understand the stability of this device configuration as it is exposed to other stressors such as clean dry air or humidity. Moving forward, the community can use such standardized tests, degradation platforms, and analysis methods to develop various hypotheses on what mechanisms are associated with the degradation modes seen in a particular device architecture, and then use postmortem analysis to confirm or deny the hypotheses. Ideally, these results, reported in the ISOS framework, can then be used to do larger data analytics across wide ranges of devices architectures to develop deeper insight.

## Author Contributions

S.R. designed the SPA flow tube units with assistance from M.O.R. and J.J.B. S.P.D. and S.R. built the SPA setup with assistance from A.E.L. and J.W. S.P.D. developed the algorithms and software used for analysis and analysed the data. A.E.L. Fabricated the cells under tests. R.T. performed the degradation tests. M.O.R. and J.J.B. supervised the project and secured funding. S.P.D. wrote the original draft. All authors contributed to review and editing.

## Conflicts of interest

S.P.D. is a technical advisor currently advising for Verde Technologies.

## Acknowledgements

This work was authored in part by the National Renewable Energy Laboratory, operated by Alliance for Sustainable Energy, LLC, for the U.S. Department of Energy (DOE) under Contract No. DE-AC36-08GO28308. All work was supported by U.S. Department of Energy Office of Energy Efficiency and Renewable Energy, Solar Energy Technologies Office (SETO) projects “De-Risking Halide Perovskite Solar Cells" and “Advanced Perovskite Cells and Modules”. The views expressed in the article do not necessarily represent the views of the DOE or the U.S. Government. The U.S. Government retains and the publisher, by accepting the article for publication, acknowledges that the U.S. Government retains a nonexclusive, paid-up, irrevocable, worldwide license to publish or reproduce the published form of this work, or allow others to do so, for U.S. Government purposes.

## Notes and references

[1] M. O. Reese, S. A. Gevorgyan, M. Jørgensen, E. Bundgaard, S. R. Kurtz, D. S. Ginley, D. C. Olson, M. T. Lloyd, P. Morvillo, E. A. Katz, A. Elschner, O. Haillant, T. R. Currier, V. Shrotriya, M. Hermenau, M. Riede, K. R. Kirov, G. Trimmel, T. Rath, O. Inganäs, F. Zhang, M. Andersson, K. Tvingstedt, M. Lira-Cantu, D. Laird, C. McGuiness, S. Gowrisanker, M. Pannone, M. Xiao, J. Hauch, R. Steim, D. M. Delongchamp, R. Rösch, H. Hoppe, N. Espinosa, A. Urbina, G. Yaman-Uzunoglu, J. B. Bonekamp, A. J. J. M. Van Breemen, C. Girotto, E. Voroshazi, F. C. Krebs, *Sol. Energy Mater. Sol. Cells* **2011**, *95*, 1253–1267.

[2] M. V Khenkin, E. A. Katz, A. Abate, G. Bardizza, J. J. Berry, C. Brabec, F. Brunetti, V. Bulović, Q. Burlingame, A. Di Carlo, R. Cheacharoen, Y. B. Cheng, A. Colsmann, S. Cros, K. Domanski, M. Dusza, C. J. Fell, S. R. Forrest, Y. Galagan, D. Di Girolamo, M. Grätzel, A. Hagfeldt, E. von Hauff, H. Hoppe, J. Kettle, H. Köbler, M. S. Leite, S. (Frank) Liu, Y. L. Loo, J. M. Luther, C. Q. Ma, M. Madsen, M. Manceau, M. Matheron, M. McGehee, R. Meitzner, M. K. Nazeeruddin, A. F. Nogueira, Ç. Odabaşı, A. Osherov, N. G. Park, M. O. Reese, F. De Rossi, M. Saliba, U. S. Schubert, H. J. Snaith, S. D. Stranks, W. Tress, P. A. Troshin, V. Turkovic, S. Veenstra, I. Visoly-Fisher, A. Walsh, T. Watson, H. Xie, R. Yıldırım, S. M. Zakeeruddin, K. Zhu, M. Lira-Cantu, *Nat. Energy* **2020**, *5*, 35–49.

[3] L. B. Miller, S. P. Donohoe, M. H. Jones, W. A. White, L. E. Klebanoff, S. A. Velinsky, *Energy Technol. Policy* **2015**, *2*, 58–72.

[4] R. Elliot, “The Lighting Pages: Lamps and Lighting,” can be found under https://sound-au.com/lamps/index.html, **2020**.

[5] Plasma Bright, “Plasma Lighting Systems,” **2010**.

[6] Plasma International, “Plasma International: Products,” **2020**.

[7] M. G. L. Gustafsson, G. H. Patterson, J. Lippincott-Schwartz, M. W. Davidson, *Zeiss* **2013**, 1–18.

[8] M. Tawfik, X. Tonnellier, C. Sansom, *Renew. Sustain. Energy Rev.* **2018**, *90*, 802–813.

[9] P. Morgan Pattison, M. Hansen, J. Y. Tsao, *Comptes Rendus Phys.* **2018**, *19*, 134–145.

[10] K. Reynolds, *Photonics Spectra* **2015**, *49*, 54–58.

[11] Glamox Technology Team, “LED Education Centre,” can be found under https://glamox.com/gsx/led, **2013**.

[12] D. L. Bubenheim, R. Sargis, D. Wilson, *HortScience* **1995**, *30*, 1086–1089.

[13] M. Cart, M. H. Lamp, “Metal Halide Lights: What are they

 

and how do they work?," can be found under https://www.shineretrofits.com/lighting-center/faq/what-is-a-metal-halide-light/, **2020**.

[14] S. H. Jeong, J. Park, T. H. Han, F. Zhang, K. Zhu, J. S. Kim, M. H. Park, M. O. Reese, S. Yoo, T. W. Lee, *Joule* **2020**, *4*, 1206–1235.

[15] N. Pellet, F. Giordano, M. Ibrahim Dar, G. Gregori, S. M. Zakeeruddin, J. Maier, M. Grätzel, *Prog. Photovoltaics Res. Appl.* **2017**, *25*, 942–950.

[16] M. Bliss, A. Smith, J. Baker, F. De Rossi, T. Watson, K. Schutt, H. Snaith, T. R. Betts, R. Gottschalg, *Photovolt. Sci. Appl. Technol.* **2018**, 5–8.

[17] A. J. Cimaroli, Y. Yu, C. Wang, W. Liao, L. Guan, C. R. Grice, D. Zhao, Y. Yan, *J. Mater. Chem. C* **2017**, *5*, 10152–10157.

[18] Z. Ni, H. Jiao, C. Fei, H. Gu, S. Xu, Z. Yu, G. Yang, Y. Deng, Q. Jiang, Y. Liu, Y. Yan, J. Huang, *Nat. Energy* **2022**, *7*, 65–73.

[19] M. Prete, M. V. Khenkin, D. Glowienka, B. R. Patil, J. S. Lissau, I. Dogan, J. L. Hansen, T. Leißner, J. Fiutowski, H. G. Rubahn, B. Julsgaard, P. Balling, V. Turkovic, Y. Galagan, E. A. Katz, M. Madsen, *ACS Appl. Energy Mater.* **2021**, *4*, 6562–6573.

[20] R. A. Z. Razera, D. A. Jacobs, F. Fu, P. Fiala, M. Dussouillez, F. Sahli, T. C. J. Yang, L. Ding, A. Walter, A. F. Feil, H. I. Boudinov, S. Nicolay, C. Ballif, Q. Jeangros, *J. Mater. Chem. A* **2020**, *8*, 242–250.

[21] *IEC 60904 Ed. 2.0 Photovoltaic Devices*, IEC Central Office, Geneva, Switzerland, **2006**.

[22] IEC, *IEC 61215: Terrestrial Photovoltaic (PV) Modules - Design Qualification and Type Approval*, IEC Central Office, Geneva, Switzerland, **2005**.

[23] X. Zhao, T. Liu, Q. C. Burlingame, T. Liu, R. Holley, G. Cheng, N. Yao, F. Gao, Y. L. Loo, *Science (80-. ).* **2022**, *377*, 307–310.